

Creep along the Imperial Fault, southern California, from GPS measurements

Suzanne N. Lyons, Yehuda Bock, and David T. Sandwell

Cecil H. and Ida M. Green Institute of Geophysics and Planetary Physics, Scripps Institution of Oceanography, La Jolla, California, USA

Received 16 July 2001; revised 13 May 2002; accepted 30 May 2002; published 23 October 2002.

[1] In May of 1999 and 2000, we surveyed with Global Positioning System (GPS) 46 geodetic monuments established by Imperial College, London, in a dense grid (half-mile spacing) along the Imperial Fault, with three additional National Geodetic Survey sites serving as base stations. These stations were previously surveyed in 1991 and 1993. The Imperial College sites were surveyed in rapid-static mode (15–20 min occupations), while the NGS sites continuously received data for 10 h d^{-1} . Site locations were calculated using the method of instantaneous positioning, and velocities were determined relative to one of the NGS base stations. Combining our results with far-field velocities from the Southern California Earthquake Center (SCEC), we fit the data to a simple elastic dislocation model with 35 mm yr^{-1} of right-lateral slip below 10 km and 9 mm yr^{-1} of creep from the surface down to 3 km. The velocity field is asymmetrical across the fault and could indicate a dipping fault plane to the northeast or a viscosity contrast across the fault. *INDEX TERMS:* 3902 Mineral Physics: Creep and deformation; 1208 Geodesy and Gravity: Crustal movements—intraplate (8110); 8010 Structural Geology: Fractures and faults; 8110 Tectonophysics: Continental tectonics—general (0905); *KEYWORDS:* creep, GPS, InSAR, southern San Andreas, permanent scatterer

Citation: Lyons, S. N., Y. Bock, and D. T. Sandwell, Creep along the Imperial Fault, southern California, from GPS measurements, *J. Geophys. Res.*, 107(B10), 2249, doi:10.1029/2001JB000763, 2002.

1. Introduction

[2] An important issue for both earthquake physics and earthquake hazards mitigation is the depth and extent of aseismic fault slip. Some faults remain locked over the entire thickness of the seismogenic zone throughout the earthquake cycle and thus can store maximum seismic moment while other faults slide freely from the surface to the base of the seismogenic zone and, therefore, may be less hazardous [Bürgmann *et al.*, 2000]. This slow movement of the Earth's surface at a fault is known as creep.

[3] Fault friction models [e.g., Weertman, 1964; Savage and Burford, 1971; Tse and Rice, 1986] relate slip at depth to surface displacement. Therefore, one can examine the spatial distribution of crustal displacement over a long period of time (>5 years) to detect the interseismic signal and determine if a fault is creeping during that time. Creep can be gradual (months to years) or it can occur in short episodes known as “creep events” (lasting hours to days). While creep meters have excellent temporal sampling, they lack the spatial coverage needed to determine the depth variations in aseismic slip. In contrast, most geodetic measurements lack temporal resolution but, if sufficiently dense, they can be used to infer the slip distribution with depth [Thatcher, 1983; Harris and Segall, 1987; Lorenzetti and Tullis, 1989; Savage, 1990; Savage and Lisowski, 1993]. Dense geodetic networks, such as the one along

the Imperial Fault in southern California [Mason, 1987], are well suited for observing the near-field spatial distribution of slip that primarily reflects the shallow component of slip on a fault.

[4] Located southwest of the Salton Sea (Figure 1), the Imperial Valley has experienced numerous large seismic episodes this century: 19 April 1906 ($M = 6.0+$), 22 June 1915 ($M_L = 6.1$ and 6.3), 28 May 1917 ($M = 5.5$), 1 January 1927 ($M = 5.8$), 19 May 1940 ($M_L = 7.1$), and 15 October 1979 ($M_L = 6.9$) [Genrich *et al.*, 1997]. Most of the motion from these earthquakes has occurred along the Imperial Fault, a right-lateral strike-slip fault which runs for 69 km through the eastern portion of El Centro and the western side of Holtville, south into the Mexicali Valley (Figure 1). A relatively fast-moving fault, the estimated average slip rate along the Imperial Fault ranges from 15–20 mm yr^{-1} based on shoreline deposits [Thomas and Rockwell, 1996] to 35–43 mm yr^{-1} based on conventional geodetic surveys [Bennett *et al.*, 1996; Genrich *et al.*, 1997; Wdowinski *et al.*, 2001]. Geodetic rates indicate the Imperial Fault accommodates almost 80% of the total plate motion between the North American and Pacific Plates. The earthquake recurrence interval for the Imperial Fault is on the order of 40 years for $M_L = 6.0$ and 700 years for $M_L = 7.0+$ [Southern California Earthquake Center (SCEC) Crustal Deformation Working Group, 1999, available at http://www.scecdc.scec.org/group_e/release.v2].

[5] The Imperial Fault was first identified from coseismic motion during the 1940 earthquake. Surface rupture from this quake occurred along more than 40 km of the trace.

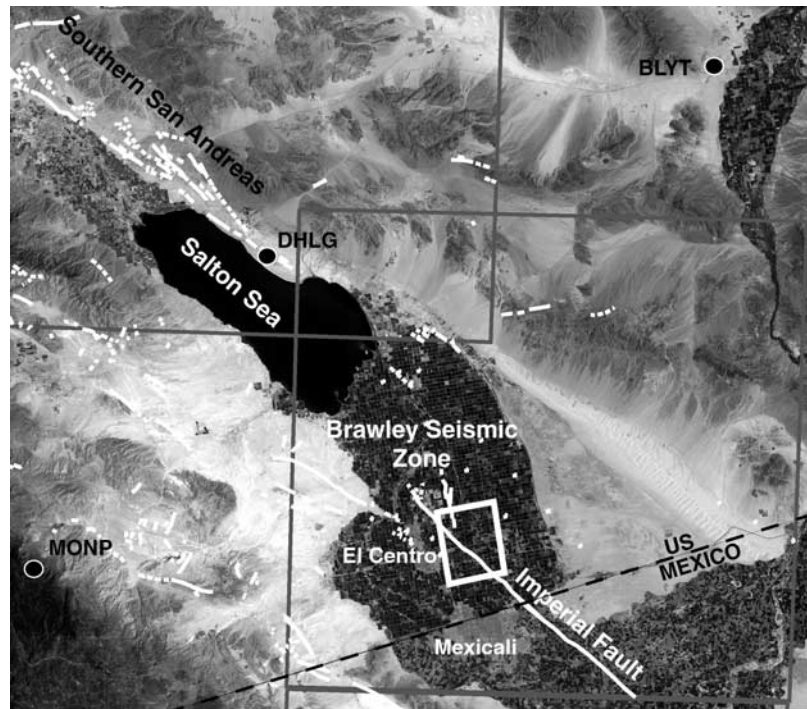


Figure 1. The Salton Sea and Imperial Valley, southern California. Major faults are in white, white box indicates GPS survey region, and large gray boxes highlight Synthetic Aperture Radar (SAR) coverage from ERS-1/2.

Ellsworth [1990] estimates 60 km of rupture, with displacement ranging from about 75 cm near El Centro to 4.5 meters at the Mexican border. Elastic half-space models were used to estimate an additional postseismic creep of 75 cm along the northern section and 1.5 m along the southern part [Reilinger, 1984].

[6] The 1979 Imperial Valley earthquake caused coseismic slip along 30.5 km of the fault trace, with geodetic data yielding displacement ranging from 13 cm along the northern and southern sections of the fault to 48 cm on a 10-km section straddling the U.S.–Mexico border [King and Thatcher, 1998]. The postseismic slip was on the order of 30 cm over the next six months [Sharp *et al.*, 1982].

[7] While it is common practice to determine slip rates and displacement during coseismic events along faults such as the Imperial [e.g., Hartzell and Heaton, 1983; Archuleta, 1984; King and Thatcher, 1998], it is the moment accumulation rate [Savage and Simpson, 1997] during the long interseismic period that may be the key to earthquake prediction. The moment accumulation rate per length of fault is proportional to the slip rate times the height of the locked portion of the fault. Most of this accumulated seismic moment (and elastic energy) is released during the infrequent major events. Thus, according to the elastic rebound theory [Reid, 1969], there is an increased likelihood of a major earthquake in regions with high localized strain rates. In creeping sections of faults, some of the accumulated shear strain is continuously released, which might lower the risk of major earthquake events. Therefore, interseismic near-field deformation characteristics of major southern California faults may provide insight into hazard assessments for this region.

[8] Wdowinski *et al.* [2001] analyzed velocities compiled by the SCEC Crustal Deformation Working Group from GPS measurements, triangulation, trilateration, and electronic distance measurements [SCEC Crustal Deformation Working Group, 1999] and found a well-defined belt of high strain rate ($0.5 \mu\text{strain yr}^{-1}$) along the Imperial Fault. This shear belt is characterized by a high level of microseismicity (>200 events in 1997 [Richards-Dinger and Shearer, 2000]), indicating that a large part of the interseismic deformation occurs within the brittle upper crust (7.5 ± 4.5 km) [Wdowinski *et al.*, 2001].

[9] Along the Imperial Fault, studies of pre-1979-earthquake slip rates using creep meter measurements [Goultly *et al.*, 1978; Cohn *et al.*, 1982; Louie *et al.*, 1985] yielded only $2\text{--}5 \text{ mm yr}^{-1}$ of fault creep. However, using EDM surveys of fault-crossing lines, Genrich *et al.* [1997] found an average of $10\text{--}14 \text{ mm yr}^{-1}$ of creep between 1987 and 1993. They attributed this high rate to triggered slip from the 1987 Superstition Hills earthquake, which would imply that current rates would be closer to pre-1979 estimates.

2. GPS Methods

[10] During the interseismic period, the relative ground motion across the fault is quite small ($<35 \text{ mm yr}^{-1}$), especially for stations close to the fault trace, so it is important to obtain precise positions. By using continuous Global Positioning System (GPS) data, it is possible to determine the location of specific points over small apertures such as the Imperial College network to millimeter accuracy and precision [Bock *et al.*, 2000]. While continu-

ous GPS has high resolution for displacement at each site, it is difficult to get effective spatial coverage without extremely dense GPS arrays. This is not too problematic in the Los Angeles basin, where taxpayers are willing to spend large amounts of money for earthquake research, but in desert areas such as the Imperial Valley, the cost of installing a dense network of permanent GPS sites becomes unrealistic. Thus, we are forced to use alternate methods for acquiring displacement data.

[11] In areas of sparse GPS, the use of interferometric SAR (InSAR, gray boxes, Figure 1) measurements seems ideally suited for observing the shallow component of fault slip [Zebker *et al.*, 1994; Peltzer *et al.*, 1996; Rosen *et al.*, 1996; Massonnet and Feigl, 1998; Vincent, 1998]. The InSAR method works well in arid regions such as north of the Salton Sea, where phase coherence is retained over long periods of time [Lyons *et al.*, 2000; Sandwell and Agnew, 1999]. However, in the farmland of the Imperial Valley, interferograms formed from available SAR images appear noisy due to the loss of phase coherence over time and it is extremely difficult to discern the near-field deformation across the faults in these areas. Therefore, we turn to a more practical method of GPS survey to obtain data in irrigated areas near major faults: the rapid-static survey.

[12] Kinematic GPS surveying yields the greatest number of observation points in the least amount of time compared to static GPS surveying. One station is “fixed” while the other receiver is moved from observation point to observation point. Kinematic GPS determines the position of this roving receiver relative to the known stationary base site at every epoch. The integer cycle, doubly differenced phase ambiguities are resolved, leaving only the three station position parameters to be solved for at each epoch [Genrich and Bock, 1992]. Using dual frequency receivers, only 1–2 min at each observation point is required to achieve relative horizontal positional accuracies at the centimeter level for baselines up to ~10 km [Hofmann-Wellenhof *et al.*, 1997]. While quite promising for maximizing the number of observation points in minimal time (important in applications such as the generation of high resolution topographic maps), kinematic GPS requires that phase lock be maintained on five or more satellites throughout the entire survey (or recovered in postprocessing). Although on-the-fly ambiguity resolution techniques are available, kinematic GPS surveying suffers from initialization and reinitialization problems that limit the ability to resolve reliably and continuously integer-cycle phase ambiguities throughout the survey [Bock *et al.*, 2000].

[13] Rapid static surveying, on the other hand, involves fast ambiguity resolution through the utilization of dual frequency receivers and good satellite geometry [Blewitt, 1993]. Thus, loss of lock does not affect the solution since the integer cycle phase ambiguities can be reacquired at any time during the survey [Genrich and Bock, 1992]. In rapid static mode, as in kinematic mode, one station is stationary while the other receiver roams from site-to-site. Genrich and Bock [1992] used a combination of kinematic and rapid static techniques to determine movement across the San Andreas Fault in central California. They showed that, by computing the baseline epoch-by-epoch after resolving for

phase ambiguities, it is possible to achieve millimeter horizontal precision with brief (~10 min) occupation times for a short-range (<1 km) survey during periods of good satellite geometry.

3. Imperial College Network

[14] Although various geodetic surveys were performed in the Imperial Valley as early as 1939, these used classic positioning techniques (trilateration and triangulation) on a coarse grouping of stations [Snay and Drew, 1988]. In the 1970s and 1980s, under a grant from the U.S. Geological Survey, the Imperial College (IC) of London constructed a dense grid of survey markers in the Imperial Valley near El Centro to monitor motion along the Imperial Fault [Mason, 1987]. This network consists of buried monuments in a pattern coinciding with agricultural roads running north–south and east–west every half mile. These stations are identified according to location: the first digit is a letter indicating the north–south position and the second two digits identify the east–west position [Crook *et al.*, 1982].

[15] Various sections of this grid have been surveyed since the last major earthquake in 1979. The most recent studies have used GPS positioning techniques and focused on the main section of the grid (Figure 2) [Genrich, 1992; Genrich *et al.*, 1997; Lyons *et al.*, 1999, 2000].

[16] The 1991 survey of Genrich [1992] included 67 IC stations with 5 local National Geodetic Survey (NGS) stations and was performed in kinematic mode, with the NGS stations serving as a static base network to maintain sufficient network control and redundancy. Unfortunately, due to poor satellite geometry, we were unable to use the data in our analysis. In 1993, Genrich *et al.* [1997] resurveyed the 72 stations using five dual-frequency, full carrier wavelength L2 codeless receivers. Due to improved receiver technology and satellite geometry, they employed the rapid-static procedure, discussed above, where integer cycle ambiguities are resolved during each session, so maintaining phase lock on the satellites in between site occupations is unnecessary.

[17] In May of 1999 and 2000, we resurveyed 46 of these sites in the IC network in rapid-static mode, with 3 additional NGS sites serving as static base stations [Lyons *et al.*, 1999, 2000]. Thirteen of the IC sites were reoccupied during each survey to determine the precision of the measurements. Occupation time at each site was 15–20 min. Three NGS stations were continuously receiving data during the 10 hours of surveying each day and provided a relative reference frame for the IC sites.

4. Data Processing

[18] Typically, the processing of field GPS data includes parameter estimation from several hour spans of data sampled every 30 s. Site positions are determined by batch least squares or other multiepoch estimation methods [e.g., Bock *et al.*, 1997]. These techniques often require many epochs of dual-frequency data in order to resolve phase ambiguities and frequently do poorly with short observation spans. Outliers due to multipath and other site-specific errors, receiver losses of lock, and phase cycle

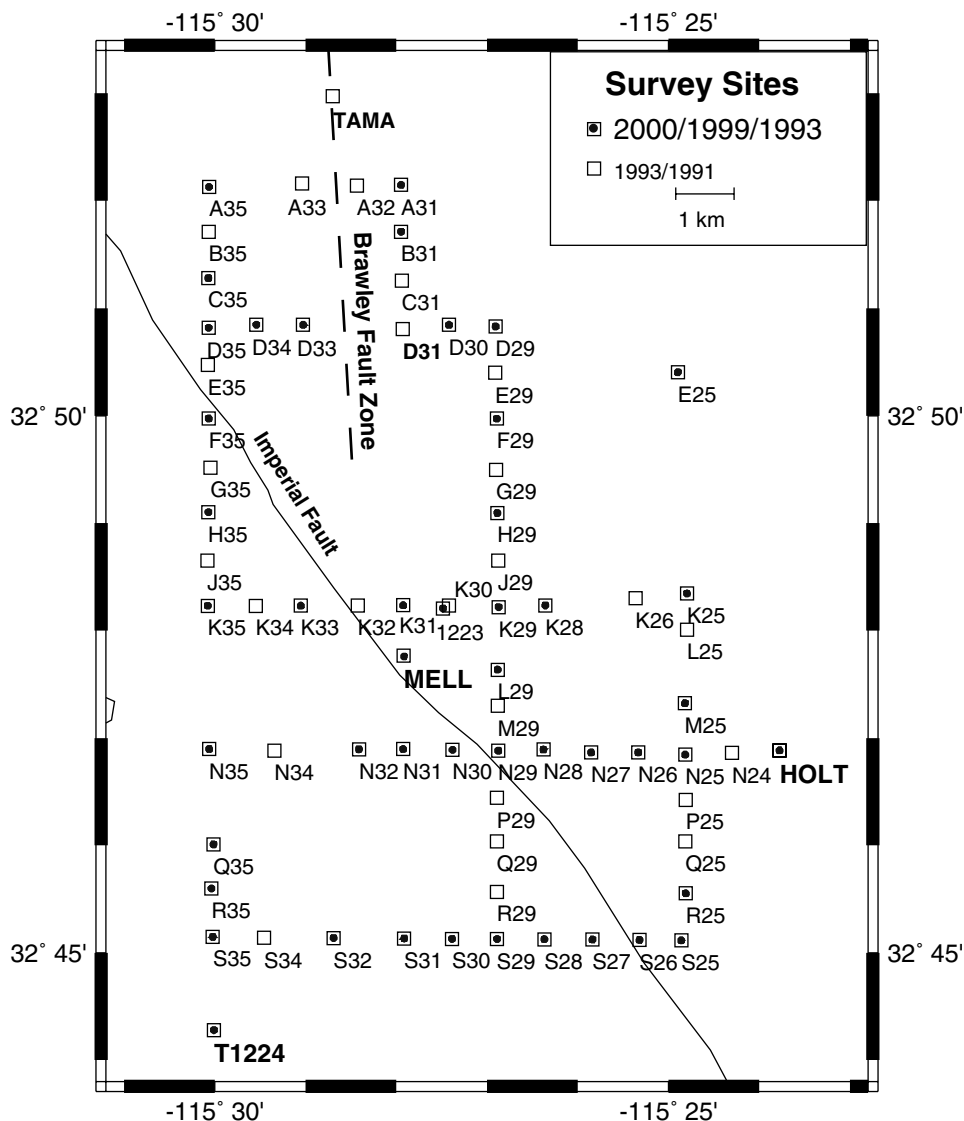


Figure 2. Sites surveyed between 1991 and 2000 along the Imperial Fault. NGS stations are shown in bold. Numbers indicate east–west position and letters indicate north–south position.

slips can strongly influence the final positioning when using these methods, by complicating reliable integer-cycle ambiguity resolution.

[19] This can be avoided by using a new method of precise GPS processing called instantaneous positioning [Bock *et al.*, 2000]. Estimates of the position of an unknown site are found relative to a known fixed site up to several tens of kilometers away with only a single epoch of data. The positions (and zenith delay parameters) are estimated independently for each observation epoch, thereby avoiding the cleaning and repairing of the input GPS observables for outliers, receiver losses of lock, and phase cycle slips. Receiver loss of lock and phase cycle slips are irrelevant at the single-epoch level since ambiguity resolution is instantaneous and independent at each epoch. Outliers are determined from the single-epoch positions using the interquartile range of the suite of solutions for that site. The interquartile range is a measure of spread or

dispersion. It is the difference between the 75th percentile (often called Q3) and the 25th percentile (Q1). The formula for the interquartile range is therefore simply $Q3 - Q1$. Although not used extensively, the interquartile range is a robust measure of scatter and is the preferred method of measuring dispersion in distributions with outliers.

[20] For short to intermediate length baselines, the instantaneous positioning method provides comparable precision to batch processing methods while requiring only a fraction of the amount of data. Since the phase ambiguities and site coordinates are determined independently at each epoch, the solution rate can equal the sampling rate. Bock *et al.* [2000] demonstrated that for small aperture networks such as the one in this study, averaging instantaneous positions estimated over a 15–20 minute interval is sufficient to achieve 1 mm horizontal position precision. Thus, for studies of fault movement in

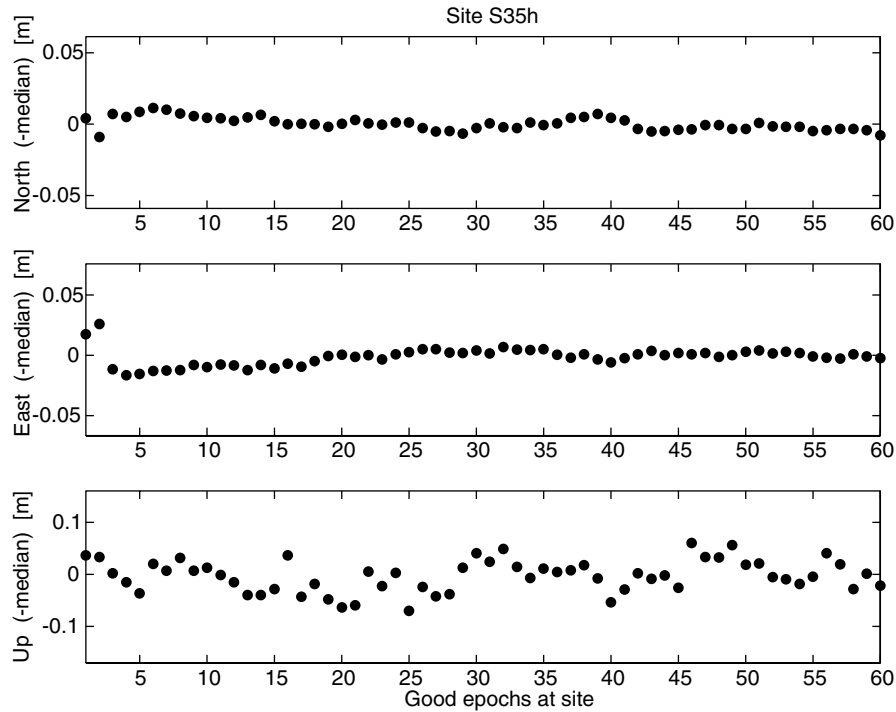


Figure 3. Independent single-epoch solutions (every 15 seconds) for baseline between sites S35 and HOLT. The horizontal single-epoch precision is 8 mm, with a decrease by a factor of 10 in the vertical. By stacking numerous epoch solutions, we can reduce the horizontal scatter to <1 mm for the base stations and ~ 2 mm for the roving stations.

regions with dense GPS networks, such as the Imperial Valley, a combination of rapid-static surveying and instantaneous positioning provides the most efficient means of precise position estimation.

5. Method

[21] Combining daily orbit solutions, our local static data, and data obtained from three Southern California Integrated GPS Network (SCIGN, <http://www.scign.org>) sites for the survey time period, we determined daily positions for the base stations using the GAMIT software [King and Bock, 1995]. The three SCIGN sites used for the 1999 and 2000 analysis were MONP, BLYT, and DHLG (Figure 1, circles). As each of these sites was installed after 1994, for the 1993 survey we used the more westerly SCIGN sites of PIN1, ROCH, SIO2 and SIO3 (<http://sopac.ucsd.edu/maps/>).

[22] Each SCIGN station was tightly constrained to its International Terrestrial Reference Frame 1996 (ITRF96) value [Sillard *et al.*, 1998], with an a priori 1 mm standard deviation in each component. The base station coordinates were allowed to adjust freely and daily base station positions were solved in batch mode relative to this SCIGN reference network. One of the base stations (HOLT) was then tightly constrained and all site data was processed epoch-by-epoch relative to the base station network. Unlike Genrich *et al.* [1997], we processed all of the survey data using instantaneous positioning (discussed above and in the work of Bock *et al.* [2000]) rather than the batch least squares method. We

defined anomalous solutions as three times the interquartile range and removed these points from the suite of position estimates at each site. Final site positions were determined by the median of the remaining estimates.

[23] Precision for a single-epoch solution is in the centimeter range, with precision for the suite of estimates at the millimeter level (Figure 3). The precision of the vertical component is generally about a factor of five to ten less than the horizontal component, so we focused on horizontal displacements. Uncertainties for the suite of estimates were ascertained using an empirical relationship derived from Bock *et al.* [2000], in which they determine the baseline scatter associated with various baseline lengths (50 m, 14 km, and 37 km) for different collection times (1, 10, 30, 120, 720, 2880, and 11,520 epochs). We used Figure 11 in the work of Bock *et al.* [2000], which shows the interquartile range for short distances based on a 12-week analysis of PIN1–PIN2 (50 m). From this, we interpolated to determine the weights for our single-epoch uncertainties based on the number of data points at each site. Sigma estimates for position were derived from this interquartile range ($\sigma = \text{IQR}/1.35$), assuming the errors were normally distributed (after outliers were excluded). For site S35 (Figure 3), the single-epoch sigma values for the north (σ_n) and east (σ_e) positions are 5.47 mm and 6.24 mm, respectively, while the vertical standard deviation (σ_u) is 32.18 mm. The standard deviations for the suite of estimates are $\sigma_n = 1.47$, $\sigma_e = 1.45$, and $\sigma_u = 11.55$ mm. Velocity errors were then defined as $\sigma_{V_N} = \frac{\sqrt{\sigma_n^2 + \sigma_{p_{23}}^2}}{T}$, where σ_{V_N} is the uncertainty in the north component of the average velocity (and likewise for the east component), determined

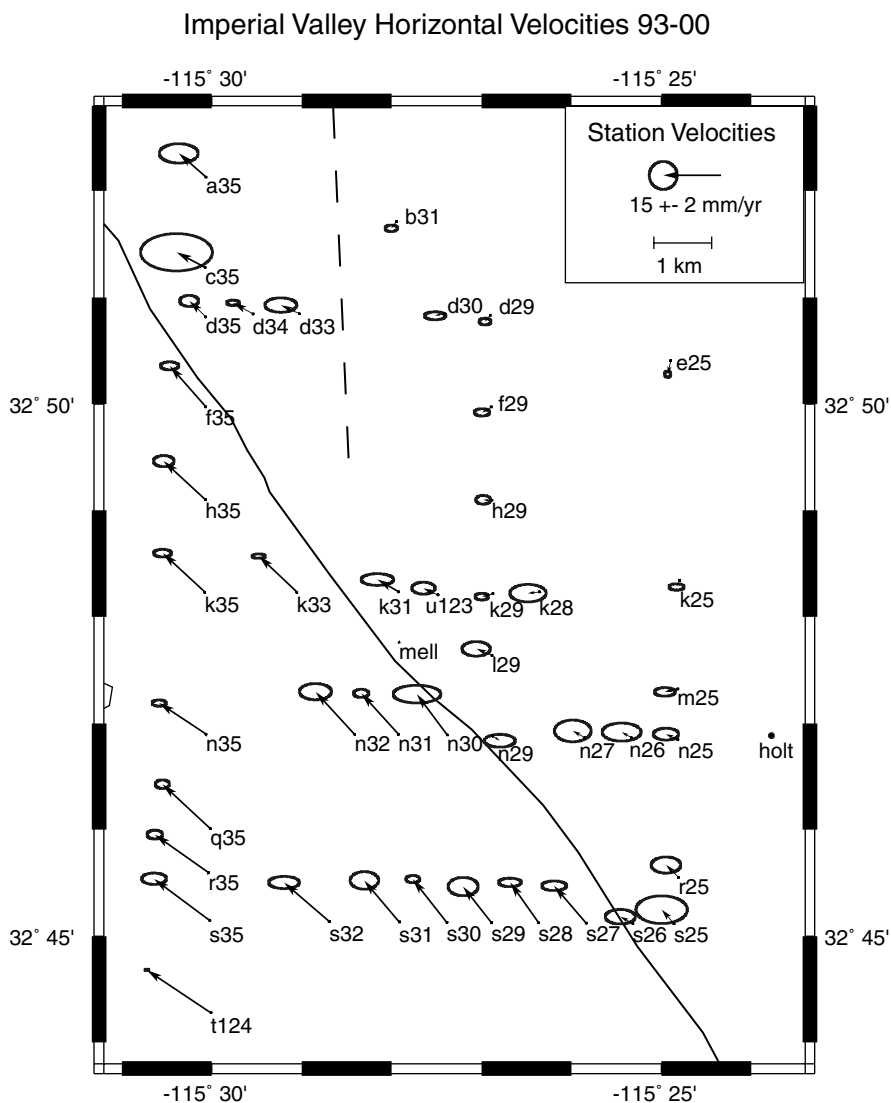


Figure 4. Average horizontal velocities between 1993 and 2000 with 95% confidence ellipses. Velocities are relative to the NGS benchmark HOLT and represent the average interseismic motion over the last decade. The velocity fields for both 1993–1999 and 1993–2000 indicate the eastern side of the fault acts as a relatively stationary block, while the western section experiences a northwesterly motion of about 15 mm yr^{-1} .

from the positional variances, $\sigma_{P1_N}^2$ and $\sigma_{P2_N}^2$, and t is the time interval (years).

6. Results

[24] Results from the 1993–2000 GPS surveys are shown in Figures 4–6. The horizontal velocity field (Figure 4) is coherent and indicates that, relative to the base station HOLT, the eastern side of the fault acts as a relatively stationary block, while the western section experiences a northwesterly motion of about 15 mm yr^{-1} . The station positions for 1993, 1999, and 2000 are consistent with linear motion of the sites over the studied time interval. Figure 5 shows the positions of four stations over the three survey years, with the best fit slope for each site. The slopes for the western sites (N30 and

Q35) are different from those of the eastern stations (B31 and S26), but all demonstrate a relatively constant velocity over the survey period.

[25] By decomposing the station velocities into their fault-normal and fault-parallel components, we can more accurately assess the nature of interseismic displacement. The fault normal velocities (Figure 6, top) indicate a small, steady compression of $\sim 3 \text{ mm yr}^{-1}$ on the eastern side of the fault, with a slight shift in velocities across the fault. The southwest corner of the survey area indicates a dilatation of $5\text{--}6 \text{ mm yr}^{-1}$. This is most likely caused by effects from the Heber Geothermal Field ($32^\circ 43' \text{N}$, $115^\circ 32' \text{W}$). *Mason* [1987] found horizontal displacements near this production zone and *Genrich et al.* [1997] attributed a westward deviation of $\sim 7 \text{ mm yr}^{-1}$ between their model and site T1224 to this geothermal area.

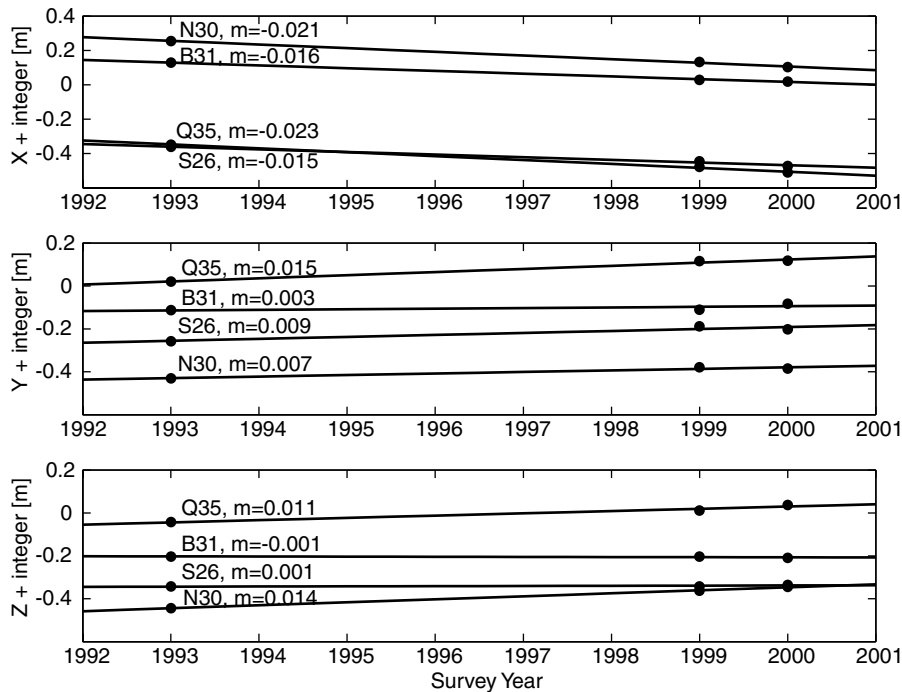


Figure 5. Relative ITRF site positions for a variety of sites in the Imperial network with least-squares “best-fit” lines. The consistency of motion in the near-field for sites on either side of the fault at both short (0.5 km, S26 and N30) and long (4.5 km, B31 and Q35) distances indicates a relatively linear motion throughout the interseismic period.

Removal of the sites near the geothermal field (thick lines west of the fault—negative orthogonal distance—in Figure 6) causes the best fit slope for the compressional component on the western side of the fault to be reduced from 0.85 to 0.29, a value that is similar to that of the eastern block of sites.

[26] The fault-parallel component (Figure 6, bottom) shows increasing velocity with distance on either side of the fault, with a jump of $\sim 9 \text{ mm yr}^{-1}$ at the fault trace. Sites in the northwest section of our survey area (thick lines east of the fault in Figure 6) appear to have the same compressional component as the surrounding region. However, the fault-parallel motion is higher than other sites east of the fault and could be due to the Brawley Seismic Zone. The Brawley Seismic Zone (BSZ) runs north–south between D33 and B31 (see Figure 2) and represents a zone of broad deformation in the region. East and southeast of the BSZ, station velocities are near zero and the velocity jump across the fault (e.g., site S26–S27) is $\sim 9.5 \text{ mm yr}^{-1}$. However, between the BSZ and the Imperial Fault, velocities reach 9 mm yr^{-1} (site A35) and the velocity jump across the fault (site C35–F35) is only $\sim 6 \text{ mm yr}^{-1}$. Thus, some of the plate motion across this boundary is accommodated in the northern section of the Imperial Fault by the Brawley Seismic Zone.

[27] Velocities for the Imperial Fault reach two-thirds of the full plate motion within 10 km of the fault. This is consistent with estimates from earlier geodetic surveys [Snay and Drew, 1988] and from the SCEC crustal motion map version 2.0 [SCEC Crustal Deformation Working Group, 1999; Wdowski et al., 2001], which revealed interplate deformation over a zone at least 50 km wide north of the

Imperial Valley and concentrated within 20 km across the Imperial Fault.

7. Fault Models

[28] To determine the variation of slip with depth using geodetic data (our GPS data plus far-field velocities derived from sparse continuous GPS coverage [SCEC Crustal Deformation Working Group, 1999]), we adopted the fault model originally proposed by Weertman [1964] and subsequently developed by Savage and Lisowski [1993]. The model consists of two plates sliding past each other with a far-field plate velocity of V . The simplest model has a fault that slips freely between minus infinity and a deep locking depth of D (Figure 7, solid curve). Our data show evidence for shallow creep between the surface of the Earth and some shallow locking depth d . We use the model of Savage and Lisowski [1993] to evaluate this shallow creep signature. In their model, shallow creep occurs when the far-field tectonic stress plus the local stress concentration due to the deep fault slip exceeds the fault strength. Fault strength depends on the coefficient of friction (~ 0.85 for most rocks [Byerlee, 1978]) times the normal stress, where normal stress has a component due to lithostatic pressure plus an unknown tectonic component of normal stress. The details of the model are found in the work of Savage and Lisowski [1993]. The unknown parameters are the deep locking depth D and the tectonic normal stress. If there is no shallow creep, the displacement follows the smooth arctangent function (Figure 7, solid curve, surface locked). If there is combined shallow slip and deep slip (Figure 7, dashed curve, surface creep), the displacement field will have a

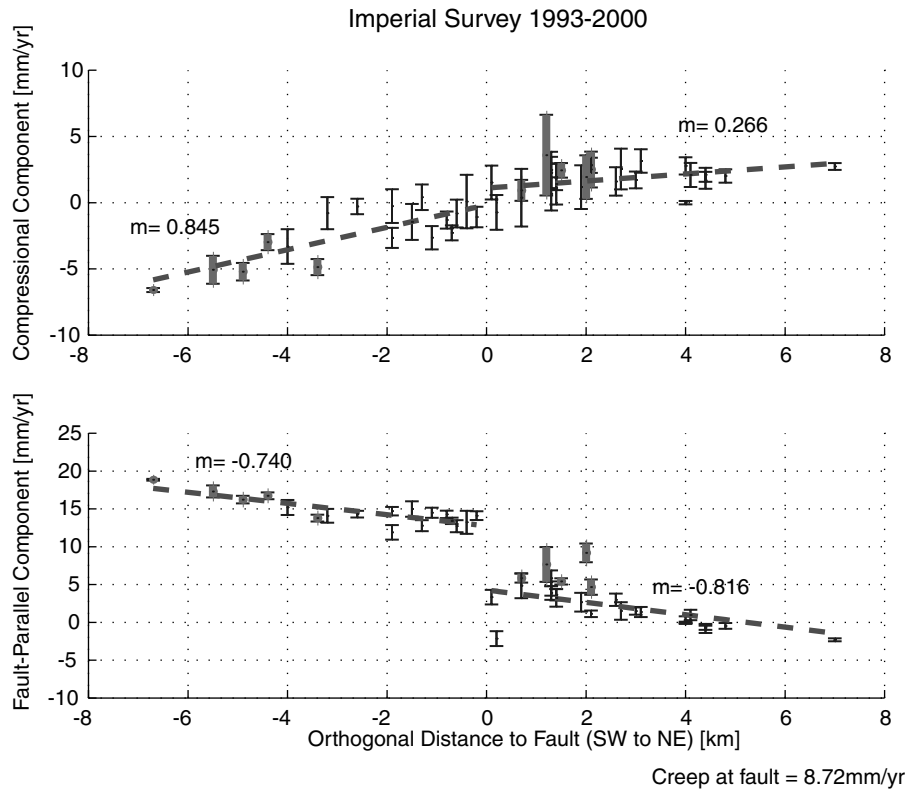


Figure 6. Average fault-parallel and fault-normal velocities versus distance from the fault for 1993–2000. Dashed lines indicate the least-squares fit, with slopes as indicated. The fault strike is defined as 323° , measured clockwise from north. The fault-normal velocities (top) indicate a small southwest component ($10 \pm 2.3 \text{ mm yr}^{-1}$) of relative motion across the entire region. Much of this could be related to the Heber Geothermal Field. See text for details. The fault-parallel component (bottom) shows increasing velocity with distance on either side of the fault, a sign of elastic strain accumulation, with a large jump in velocities at the fault, indicating creep of $9.0 \pm 1.4 \text{ mm yr}^{-1}$. Results for 1993–1999 are similar.

local abrupt transition superimposed on the broad displacement field.

[29] We varied the deep locking depth (7 to 15 km) and the tectonic normal stress (-10 to 50 MPa) to find the corresponding creeping depths. Based on previous estimates of the secular slip rate on the Imperial Fault [Bennett *et al.*, 1996; Working Group on California Earthquake Probabilities, 1995], we used $V = 35 \text{ mm yr}^{-1}$. We estimated the slip rate on the surface at the fault trace to be 9 mm yr^{-1} , (Figure 6) and then calculated the stress rate for each $D-d$ pair from Savage and Lisowski [1993] equation A13. We determined the surface velocity caused by the slip on the upper segment of the fault and calculated the rms-misfit to the geodetic measurements (plus an unknown constant).

[30] Figure 8 shows the RMS misfit between the GPS-derived velocities and the forward models for the range of locking depths and corresponding creeping depths. The minimum misfit values for $D = 8-12 \text{ km}$ are plotted as crosses, with the minimum misfit for all models at $D = 10 \text{ km}$, $d = 2.9 \text{ km}$ (star). The dashed contour line represents the minimum RMS value plus 10% and illustrates that there is a wide range of “reasonable” models for our data. The corresponding best fit forward models for $D = 8-12 \text{ km}$ are shown in Figure 9, along with the minimum misfit model for a noncreeping fault ($D = 7 \text{ km}$, $\text{RMS} = 0.43$). The

creeping models have a lower misfit than the model without creep and are more consistent with the overall deformation pattern across the fault. However, it is difficult to distinguish between the creeping models, indicating a range of locking and creeping depths that fit the geodetic data.

[31] Thus, we look at the strain rate for a range of deep slip rates and depths ($\mu = 30 \text{ GPa}$). This is shown in Figure 10, with the expected strain rates for our minimum misfit models plotted as crosses. The study by Wdowinski *et al.* [2001], which used the SCEC velocity field, version 2.0 [SCEC Crustal Deformation Working Group, 1999] to determine the shear strain rates along the San Andreas Fault System, revealed a well-defined belt of high strain rate along the Imperial Fault, with a maximum strain of $\dot{\epsilon}_{max} = 0.53 \mu\text{strain yr}^{-1}$. The shaded box in Figure 10 represents models which would produce strain rates of $0.3-0.53 \mu\text{strain yr}^{-1}$ for $V = 30-40 \text{ mm yr}^{-1}$. Our minimum misfit model for $D = 10 \text{ km}$, $d = 2.9 \text{ km}$ (best fit for all models) is the only one that coincides with this shaded region. Therefore, we choose this as the most reasonable model for the Imperial Fault.

8. Discussion

[32] The pattern of deformation across the Imperial Fault indicates that there is combined shallow slip and deep slip

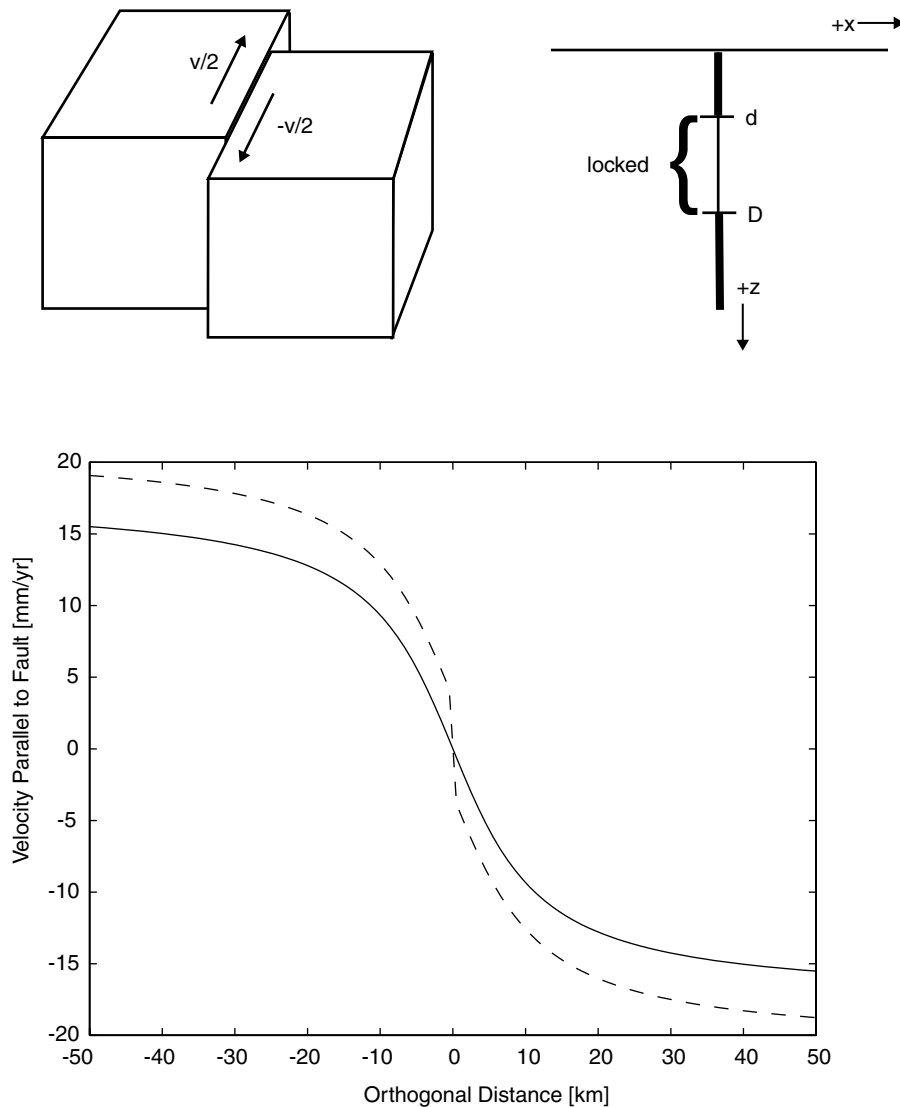


Figure 7. Elastic dislocation model using the model of *Savage and Lisowski* [1993]. (top) A right-lateral, strike-slip fault in which two blocks slide past each other with velocity V . (bottom) The resultant deformation signature across the fault if (solid line) the fault is locked from the surface to depth D and slips freely below D , and if (dashed line) the fault is locked only between d and D .

(Figure 9). However, the deformation is not symmetrical across the fault, which could indicate that the fault plane is dipping to the northeast. Previous refraction surveys [*Fuis et al.*, 1982] along the Imperial Fault, along with strong ground motion data [*Archuleta*, 1984] from the 1979 Imperial Valley earthquake and subsequent elevation surveys [*Reilinger and Larsen*, 1986] indicate that this section of the fault is dipping 80° down to the east. However, there are not enough data points east of the fault (only one station 20–60 km from the fault) for us to determine this with any certainty.

[33] Another possible explanation for the asymmetry can be inferred from *Malservisi et al.* [2001], who showed that, for the Eastern California Shear Zone (ECSZ), a high viscosity contrast between the Basin and Range Province and the Sierra Nevada block produces an asymmetric surface velocity field across this region. While the eastern

“weak” side of the ECSZ appears to accommodate most of the deformation in the region, the cold western side behaves as a strong, almost rigid block, with a flat velocity field 20–100 km from the fault and a steep gradient within 20 km of the fault. This is similar to what we see along the Imperial Fault (Figure 9), with the southwestern side of the fault appearing to behave in a weaker fashion than the northeastern side. Without more knowledge of the heat flow within this region and more detailed modeling, however, it is difficult to discern whether heat flow, fault geometry, or a combination of the two contributes to the asymmetric deformation across the Imperial Fault.

[34] Fitting frictional fault models to the data, we find that the data fits well with a model in which the Imperial Fault is creeping down to ~ 3 km at a surface rate of 9 mm yr^{-1} , with 35 mm yr^{-1} of right-lateral free slip below

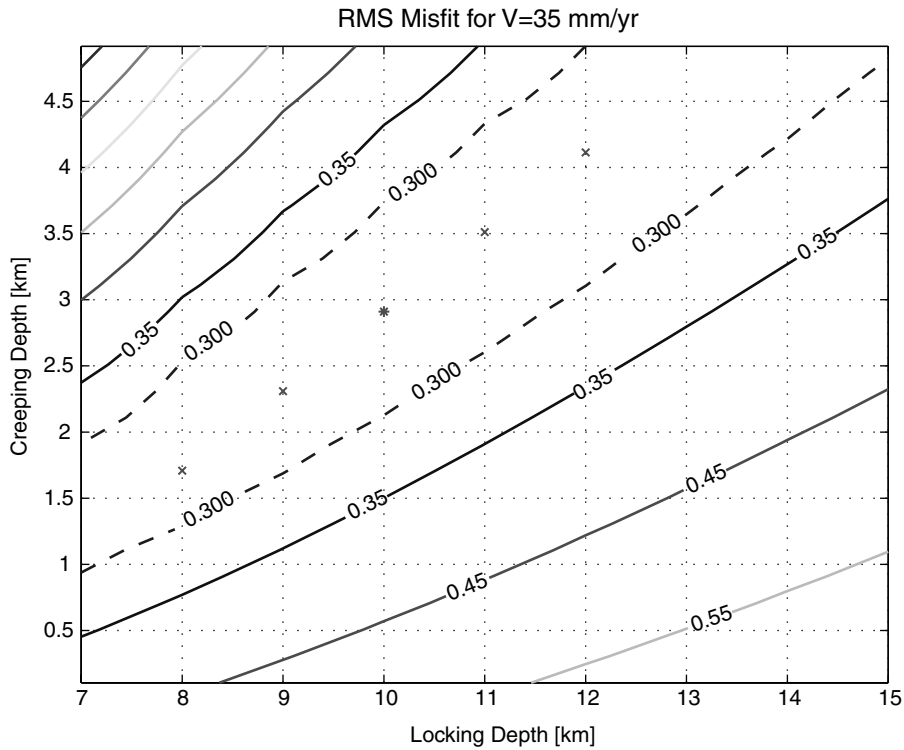


Figure 8. RMS misfit for models with varying locking depths and creeping depths. Crosses indicate the minimum misfit models at $D = 8-12$ km. Star ($D = 10$ km) is the minimum misfit of all models.

10 km. The locking depth is similar to the best fit models from 1979 coseismic data [Olson and Apsel, 1982; Hartzell and Helmberger, 1982; Hartzell and Heaton, 1983; King and Thatcher, 1998]

and is consistent with prior GPS results [Genrich *et al.*, 1997] and seismicity catalogs [Johnson and Hill, 1982; Richards-Dinger and Shearer, 2000]. The creep rate is higher than previous studies of pre-1979 earthquake rates using creep meter measurements

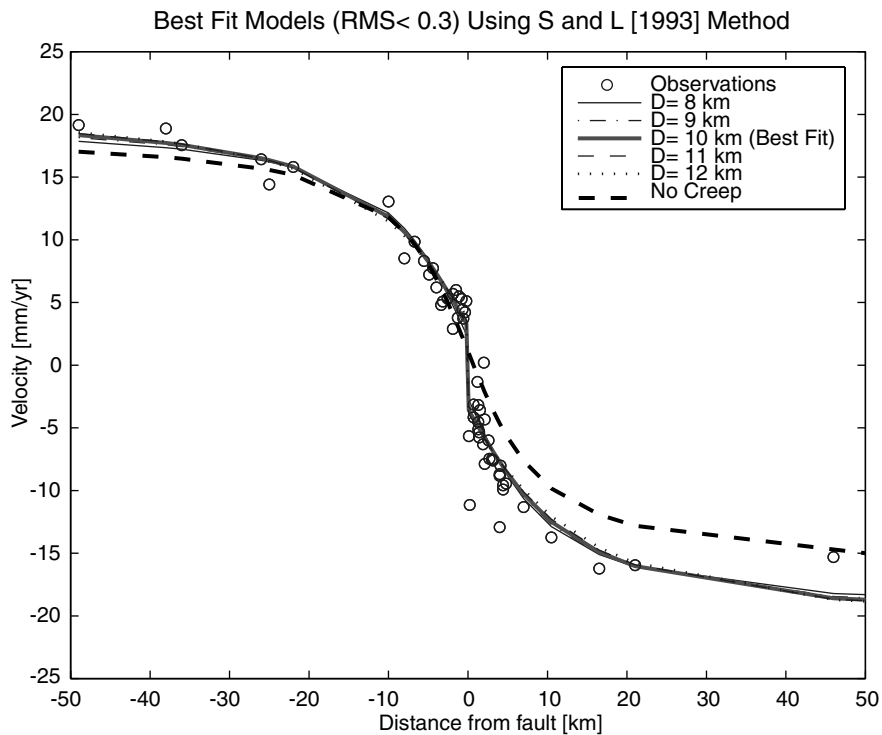


Figure 9. Minimum misfit models from Figure 8, plotted with average fault-parallel velocities with distance from the fault (circles) from both our surveys (near-field <10 km) and the SCEC estimates (far-field >10 km). Dashed line is minimum misfit model without creep.

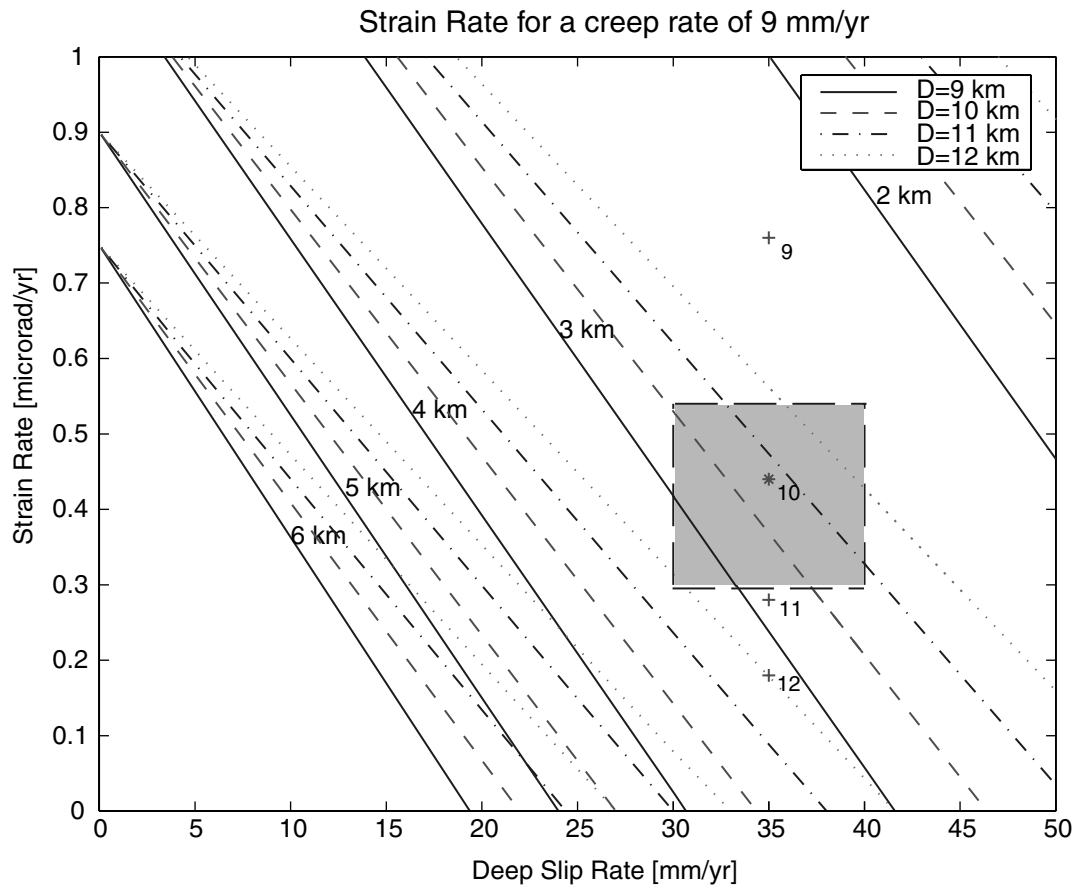


Figure 10. Strain rate estimates for various fault models. Minimum misfit models from Figure 8 are plotted as crosses, with best-fit model represented by the star. Shaded region coincides with strain estimates for the Imperial Fault from *Wdowinski et al.* [2001].

(2–5 mm yr⁻¹) [Gouly *et al.*, 1978; Cohn *et al.*, 1982; Louie *et al.*, 1985] and is closer to the post-Superstition Hills estimates by Genrich *et al.* [1997].

9. Conclusions

[35] By investigating the creep characteristics over different faults in southern California, it might be possible to discern characteristics specific to certain fault types. The tectonic implications of fault creep are still debated, with some investigators believing creep is the first step in failure leading to major earthquakes (pre-seismic slip) [Nason, 1973], while others argue that creep reduces stress buildup along faults, therefore precluding very large earthquakes along the creeping section [Prescott and Lisowski, 1983; Bürgmann *et al.*, 2000]. Regardless, most models of earthquake generation use creep to load asperities on a fault, which subsequently fail in earthquakes. Thus, creep studies are important in determining seismic hazard along active faults in southern California.

[36] The density of GPS measurements along the Imperial Fault makes it possible for us to assess the nature of the near-field motion of this fault over time. Our results for the Imperial Fault show a coherent velocity field in which the fault has been creeping 9 mm yr⁻¹ over the last

decade. The increase in creep rate since 1979 could be due to an underestimate in creep rates caused by the use of creep meters in earlier studies versus our geodetic means, as has been reported by Lisowski and Prescott [1981] and Langbein *et al.* [1983]. However, it may also imply a longer-term increase in creep rates since the last major earthquake and a corresponding decrease in the hazard for another major earthquake along this section of the Imperial Fault.

[37] Our next step will be to use Interferometric Synthetic Aperture Radar (InSAR) and permanent scatterers [Haynes, 1999; Ferretti *et al.*, 2000, 2001] along the Imperial and Cerro Prieto Faults, to look at the entire deformation field in these regions. By comparing the InSAR results with our GPS measurements and an updated SCEC crustal motion map (version 3.0), we should get a clearer indication of the behavior of these major faults in southern California and, perhaps, the risk associated with them.

[38] **Acknowledgments.** The authors would like to thank the numerous students who comprised the Imperial Fault survey teams of 1999 and 2000. Some of the figures were created using the GMT software of Wessel and Smith [1991]. Reviews by Roland Bürgmann, Tim Dixon, and Mike Lisowski led to a considerable improvement in our slip model and in the final version of this paper. This work was supported by a Department of Defense, National Defense Science and Engineering Graduate Fellowship (S. N. Lyons), NASA Earth Systems Science Fellowship (S. N. Lyons), and NSF Earth Sciences grant NSF EAR-0105896 (D. T. Sandwell). This

research was also supported by the Southern California Earthquake Center. SCEC is funded by NSF Cooperative Agreement EAR-8920136 and USGS Cooperative Agreements 14-08-0001-A0899 and 1434-HQ-97AG01718. The SCEC contribution number for this paper is 681.

References

- Archuleta, R. J., A faulting model for the 1979 Imperial Valley earthquake, *J. Geophys. Res.*, **89**, 4559–4585, 1984.
- Bennett, R. A., W. Rodi, and R. E. Reilinger, Global Positioning System constraints on fault slip rates in southern California and northern Baja, Mexico, *J. Geophys. Res.*, **101**, 21,943–21,960, 1996.
- Blewitt, G., Advances in Global Positioning System technology for geodynamics investigations: 1978–1992, in *Contributions of Space Geodesy to Geodynamics Technology, Geodyn. Ser.*, vol 25, edited by D. E. Smith and D. L. Turcotte, pp. 195–213, AGU, Washington, D. C., 1993.
- Bock, Y., et al., Southern California Permanent GPS Geodetic Array: Continuous measurements of crustal deformation between the 1992 Landers and 1994 Northridge earthquakes, *J. Geophys. Res.*, **102**, 18,013–18,033, 1997.
- Bock, Y., R. Nikolaidis, P. J. de Jonge, and M. Bevis, Instantaneous geodetic positioning at medium distances with the Global Positioning System, *J. Geophys. Res.*, **105**, 28,223–28,253, 2000.
- Bürgmann, R., D. Schmidt, R. M. Nadeau, M. d'Alessio, E. Fielding, D. Manaker, T. V. McEvilly, and M. H. Murray, Earthquake potential along the northern Hayward fault, California, *Science*, **289**, 1178–1182, 2000.
- Byerlee, J. D., Friction of rocks, *Pure Appl. Geophys.*, **116**, 615–626, 1978.
- Cohn, S. N., C. R. Allen, R. Gilman, and N. R. Gouly, Preearthquake and postearthquake creep on the Imperial Fault and the Brawley fault zone, in *The Imperial Valley, California, Earthquake of October 15, 1979, U.S. Geol. Surv. Prof. Pap.*, **1254**, 15–24, 1982.
- Crook, C. N., R. G. Mason, and P. R. Wood, Geodetic measurements of horizontal deformation on the Imperial Fault, *U.S. Geol. Surv. Prof. Pap.*, **1254**, 183–191, 1982.
- Ellsworth, W. L., Earthquake history, 1769–1989, in *The San Andreas Fault System, California*, edited by R. E. Wallace, *U.S. Geol. Surv. Prof. Pap.*, **1515**, 152–187, 1990.
- Ferretti, A., C. Prati, and F. Rocca, Nonlinear subsidence rate estimation using permanent scatterers in differential SAR interferometry, *IEEE Trans. Geosci. Remote Sens.*, **38**, 2202–2212, 2000.
- Ferretti, A., C. Prati, and F. Rocca, Permanent scatterers in SAR interferometry, *IEEE Trans. Geosci. Remote Sens.*, **39**, 8–20, 2001.
- Fuis, G. S., W. D. Mooney, J. H. Healey, G. A. McMechan, and W. J. Lutter, Crustal structure of the Imperial Valley region, *U.S. Geol. Surv. Prof. Pap.*, **1254**, 25–50, 1982.
- Genrich, J. F., Geophysical applications of GPS kinematic techniques, Ph.D. thesis, Univ. of Calif., San Diego, 1992.
- Genrich, J. F., and Y. Bock, Rapid resolution of crustal motion at short ranges with the Global Positioning System, *J. Geophys. Res.*, **97**, 3261–3269, 1992.
- Genrich, J. F., Y. Bock, and R. G. Mason, Crustal deformation across the Imperial Fault: Results from kinematic GPS surveys and trilateration of a densely-spaced, small-aperture network, *J. Geophys. Res.*, **102**, 4985–5004, 1997.
- Gouly, N. R., R. O. Burford, C. R. Allen, R. Gilman, C. E. Johnson, and R. P. Keller, Large creep events on the Imperial Fault, California, *Bull. Seismol. Soc. Am.*, **68**, 517–521, 1978.
- Harris, R. A., and P. Segall, Detection of a locked zone at depth on the Parkfield, California, segment of the San Andreas fault, *J. Geophys. Res.*, **92**, 7945–7962, 1987.
- Hartzell, S. H., and T. H. Heaton, Inversion of strong ground motion and teleseismic waveform data for the fault rupture history of the 1979 Imperial Valley, California, earthquake, *Bull. Seismol. Soc. Am.*, **73**, 1553–1583, 1983.
- Hartzell, S. H., and D. V. Helmberger, Strong-motion modeling of the Imperial Valley earthquake of 1979, *Bull. Seismol. Soc. Am.*, **72**, 571–596, 1982.
- Haynes, M., New developments in wide-area precision surveying from space, *Mapp. Aware.*, **13**, 40–43, 1999.
- Hofmann-Wellenhof, B., H. Lichtenegger, and J. Collins, *GPS: Theory and Practice*, 389 pp., Springer-Verlag, New York, 1997.
- Johnson, C. E., and D. P. Hill, Seismicity of the Imperial Valley, in *The Imperial Valley, California, Earthquake of October 15, 1979, U.S. Geol. Surv. Prof. Pap.*, **1254**, 15–24, 1982.
- King, N. E., and W. Thatcher, The coseismic slip distributions of the 1940 and 1979 Imperial Valley, California, earthquakes and their implications, *J. Geophys. Res.*, **103**, 18,069–18,086, 1998.
- King, R. W., and Y. Bock, *Documentation of the GAMIT GPS Analysis Software, v.9.4*, Mass. Inst. of Technol., Cambridge, 1995.
- Langbein, J., A. McGarr, M. J. S. Johnston, and P. W. Harsh, Geodetic measurements of postseismic crustal deformation following the 1979 Imperial Valley earthquake, California, *Bull. Seismol. Soc. Am.*, **73**, 1203–1224, 1983.
- Lisowski, M., and W. H. Prescott, Short-range distance measurements along the San Andreas fault system in central California, 1975 to 1979, *Bull. Seismol. Soc. Am.*, **71**, 1607–1624, 1981.
- Louie, J. N., C. R. Allen, D. C. Johnson, P. C. Haase, and S. N. Cohn, Fault slip in Southern California, *Bull. Seismol. Soc. Am.*, **75**, 811–833, 1985.
- Lorenzetti, E., and T. E. Tullis, Geodetic predictions of strike-slip fault model: Implications for intermediate- and short-term earthquake prediction, *J. Geophys. Res.*, **94**, 12,343–12,361, 1989.
- Lyons, S. N., Y. Bock, and R. Nikolaidis, Rapid static GPS surveys of the Imperial Fault, Southern California, *Eos Trans. AGU*, **80**, Fall Meet. Suppl., F268, 1999.
- Lyons, S. N., Y. Bock, and D. T. Sandwell, Near-field crustal deformation and creep characteristics in the Imperial Valley, *Eos Trans. AGU*, **81**, Fall Meet. Suppl., F328, 2000.
- Malservisi, R., K. P. Furlong, and T. H. Dixon, Influence of the earthquake cycle and the lithospheric rheology on the dynamics of the Eastern California shear zone, *Geophys. Res. Lett.*, **28**, 2731–2734, 2001.
- Mason, R. G., Geomensor surveys in the Imperial Valley, California, report, Geol. Dep., Imperial College, London, 1987.
- Massonnet, D., and K. L. Feigl, Radar interferometry and its applications to changes in the Earth's surface, *Rev. Geophys.*, **36**, 441–500, 1998.
- Nason, R. D., Fault creep and earthquakes on the San Andreas Fault, in *Proceedings of the Conference of Tectonic Problems of the San Andreas Fault System*, edited by R. L. Kovach and A. Nur, *Stanford Univ. Publ. Geol. Sci.* **13**, 275–285, 1973.
- Olson, A. H., and R. J. Apse, Finite faults and inverse theory with applications to the 1979 Imperial Valley earthquake, *Bull. Seismol. Soc. Am.*, **72**, 1969–2001, 1982.
- Peltzer, G., P. Rosen, F. Rogez, and K. Hudnut, Postseismic rebound in fault step-overs caused by pore fluid flow, *Science*, **273**, 1202–1204, 1996.
- Prescott, W. H., and M. Lisowski, Strain accumulation along the San Andreas Fault system east of San Francisco Bay, California, *Tectonophysics*, **97**, 41–56, 1983.
- Reid, H. F., The mechanics of the earthquake, in *The California Earthquake of April 18, 1906, Report of the State Earthquake Investigation Commission*, vol. 2, *Carnegie Inst. Washington Publ.* **87**, 192 pp., 1910. (Reprinted, 1969.)
- Reilinger, R., Coseismic and postseismic vertical movements associated with the 1940 M 7.1 Imperial Valley, California, earthquake, *J. Geophys. Res.*, **89**, 4531–4537, 1984.
- Reilinger, R., and S. Larsen, Vertical crustal deformation associated with the 1979 M = 6.6 Imperial Valley, California earthquake: Implications for fault behavior, *J. Geophys. Res.*, **91**, 14,044–14,056, 1986.
- Richards-Dinger, K. B., and P. M. Shearer, Earthquake locations in southern California obtained using source specific station terms, *J. Geophys. Res.*, **105**, 10,939–10,960, 2000.
- Rosen, P. A., S. Hensley, H. A. Zebker, F. H. Webb, and E. Fielding, Surface deformation and coherence measurements of Kilauea Volcano, Hawaii from SIR-C radar interferometry, *J. Geophys. Res.*, **101**, 23,109–23,125, 1996.
- Sandwell, D., and D. Agnew, Strain accumulation and fault creep on the southern San Andreas Fault: 1992 to present, *Eos Trans. AGU*, **80**, Fall Meet. Suppl., F692, 1999.
- Savage, J. C., Equivalent strike-slip earthquake cycles in half-space and lithosphere–asthenosphere earth models, *J. Geophys. Res.*, **95**, 4873–4879, 1990.
- Savage, J. C., and R. O. Burford, Discussion of paper by C. H. Scholz and T. J. Fitch, Strain accumulation along the San Andreas Fault, *J. Geophys. Res.*, **76**, 6469–6479, 1971.
- Savage, J. C., and M. Lisowski, Inferred depth of creep on the Hayward Fault, central California, *J. Geophys. Res.*, **98**, 787–793, 1993.
- Savage, J. C., and R. W. Simpson, Surface strain accumulation and the seismic moment tensor, *Bull. Seismol. Soc. Am.*, **87**, 1354–1361, 1997.
- Sharp, R. V., et al., Surface faulting in the central Imperial Valley, in *The Imperial Valley, California, Earthquake, October 15, 1979, U.S. Geol. Surv. Prof. Pap.*, **1254**, 119–144, 1982.
- Sillard, P., Z. Altamimi, and C. Boucher, The ITRF96 realization and its associated velocity field, *Geophys. Res. Lett.*, **25**, 3223–3226, 1998.
- Snay, R. A. and A. R. Drew, Supplementing geodetic data with prior information for crustal deformation in the Imperial Valley, California, *Tech. Rep. No. 6*, Univ. of Stuttgart, Stuttgart, Germany, 1988.
- Southern California Earthquake Center (SCEC) Crustal Deformation Working Group, SCEC horizontal deformation map v.2.0, Los Angeles, 1999.
- Thatcher, W., Nonlinear strain buildup and the earthquake cycle on the San Andreas Fault, *J. Geophys. Res.*, **88**, 5893–5902, 1983.
- Thomas, A. P., and T. K. Rockwell, A 300- to 500-year history of slip on

- the Imperial Fault near the U.S.–Mexico border: Missing slip at the Imperial fault bottleneck, *J. Geophys. Res.*, *101*, 5987–5997, 1996.
- Tse, S. T., and J. R. Rice, Crustal earthquake instability in relation to depth variation of frictional slip parameters, *J. Geophys. Res.*, *91*, 9452–9572, 1986.
- Vincent, P., Application of SAR interferometry to low-rate crustal deformation, Ph.D. thesis, Univ. of Colo., Boulder, 1998.
- Wdowinski, S., Y. Sudman, and Y. Bock, Distribution of interseismic deformation along the San Andreas fault system, southern California, *Geophys. Res. Lett.*, *28*, 2321–2324, 2001.
- Weertman, J., Continuous distribution of dislocations on faults with finite friction, *Bull. Seismol. Soc. Am.*, *54*, 1035–1058, 1964.
- Wessel, P., and W. H. F. Smith, Free software helps map and display data, *Eos Trans. AGU*, *72*, 445–446, 1991.
- Working Group on California Earthquake Probabilities, Seismic hazard in southern California: Probable earthquakes, 1994 to 2024, *Bull. Seismol. Soc. Am.*, *85*, 379–439, 1995.
- Zebker, H. A., P. A. Rosen, R. M. Goldstein, A. Gabriel, and C. L. Werner, On the derivation of coseismic displacement fields using differential radar interferometry: The Landers earthquake, *J. Geophys. Res.*, *99*, 19,617–19,643, 1994.
-
- S. N. Lyons, Y. Bock, and D. T. Sandwell, Cecil H. and Ida M. Green Institute of Geophysics and Planetary Physics, Scripps Institution of Oceanography, La Jolla, CA, USA.